6.1 Introduction

Ruddlesden Popper oxides were formed a K_2NiF_4-type structure with chemical formula $A_{n+1}B_nO_{3n+1}$, where n=1, 2, 3, etc. [194]. Various types of layered perovskite oxide materials are widely studied for different kinds of application due to their interesting optical, electrical, and magnetic properties [76, 102, 210, 229, 257, 258]. Rare earth based manganite (Ln_2MnO_4, Ln=La, Pr, Nd) has found to be extensively studied for magnetoresistance application. Partial substitution of lanthanide by alkaline earth metal improved their magnetoresistance behaviour because of the creation of oxygen vacancies to maintain the charge neutrality [75]. The ferrite series of Sr_2FeO_4, $Sr_3Fe_2O_7$ have been shown antiferromagnetic behaviour due to magnetic interaction between the partial sites of Fe^{2+}, Fe^{3+}, Fe^{4+} and oxygen vacancies [79]. The magnetic properties of oxide ceramics are further modified by partial substitution of 3d transition metals (Ni^{3+}, Co^{3+}, Fe^{3+}, etc.) due to presence of unpaired spin in their outer most orbit, known as dilute magnetic semiconductor (DMS) [45, 259, 260]. Similar to transition metal rare earth ion also possess unpaired spin in their f-orbit which is shielded by s-orbit exhibit magnetic interaction. Various lanthanides ion (Gd^{3+}, Nd^{3+}, Pr^{3+}, etc.) doped in oxides like ZnO [259], TiO_2 [261], SnO_2 [262], $BaTiO_3$ [263], $BaSnO_3$ [264], $SrSnO_3$ [265] exhibit excellent magnetic properties for the use of spintronics application. Alkaline earth based orthostannates (M_2SnO_4: M=Ca, Sr, Ba) have been widely studied as a host materials for different phosphors applications [131, 132, 266]. There are no reports available on magnetic properties of M_2SnO_4 doped with lanthanides or transition metal, so in this work the properties of Sr_2SnO_4 is modified for DMS and spintronic applications.

Meanwhile, Sr_2SnO_4 is a semiconductor used as important host material for doping of various transition metals and rare earth ions. Lanthanide ions possessing special 4f intrashells structure which makes them excellent candidate for luminescence centre in Sr_2SnO_4 layered

perovskite oxides [266]. Recently, Nd-doped semiconductors was in focus due to their unique optical properties and for their use in optoelectronic and magnetic devices [267]. Limited work have been made on the optical properties of Nd-doped Sr_2SnO_4 [268, 269]. Nd doped samples exhibited interesting optical properties useful for IR detectors [266].

In this chapter, we studied the optical and magnetic properties of $Sr_{2-x}Nd_xSnO_4$ ($0< x< 0.10$). To the best of our knowledge no reports are available on effect of Nd doping on magnetic properties of Sr_2SnO_4.

6.2 Results and Discussions

In present discussion, the system $Sr_{2-x}Nd_xSnO_4$ is abbreviated as SSN and the compositions with x=0, 0.01, 0.02, 0.04, 0.06 and 0.10 of this system are abbreviated as SSN0, SSN1, SSN2, SSN4, SSN6 and SSN10, respectively throughout the discussion of results.

6.2.1 Phase Formation and Structural Characterization using XRD

As described in TGA DSC analysis of the mixture of raw materials discussed in Chapter 3, the reaction among the raw materials to form Sr_2SnO_4 take place at 1000^oC. Therefore, all compositions of system SSN have been synthesized at 1000^oC. The obtained powders have been characterized using powder X-ray diffraction analysis. X-ray diffraction pattern of all the compositions are shown in Figure 6.1(a). The diffraction peaks are matched with the COD-1539931 of Sr_2SnO_4. Absence of any peaks related to raw materials or secondary pyrochloro phase confirmed the formation of single phase solid solution for all the compositions. Further, to determine the structural parameters like lattice parameters, bond length, bond angle and their occupancy are determined by Rietveld refinement of XRD data of all samples. Detailed procedure of Rietveld refinement is already discussed in Chapter 3. In Figure 6.1(b) refined pattern and experimental profile are shown by solid line and symbol respectively. The quality of fitting has been judged by calculating S parameter, which is

defined by ratio of weight pattern profile (R_{wp}) to experimental pattern profile (R_{exp}). The value of S close to 1 indicates that refined pattern is well fitted to the experimental data points and the parameters determined from refinement are reliable [173]. Various structural parameters obtained from refinement are given in Table 6.1.

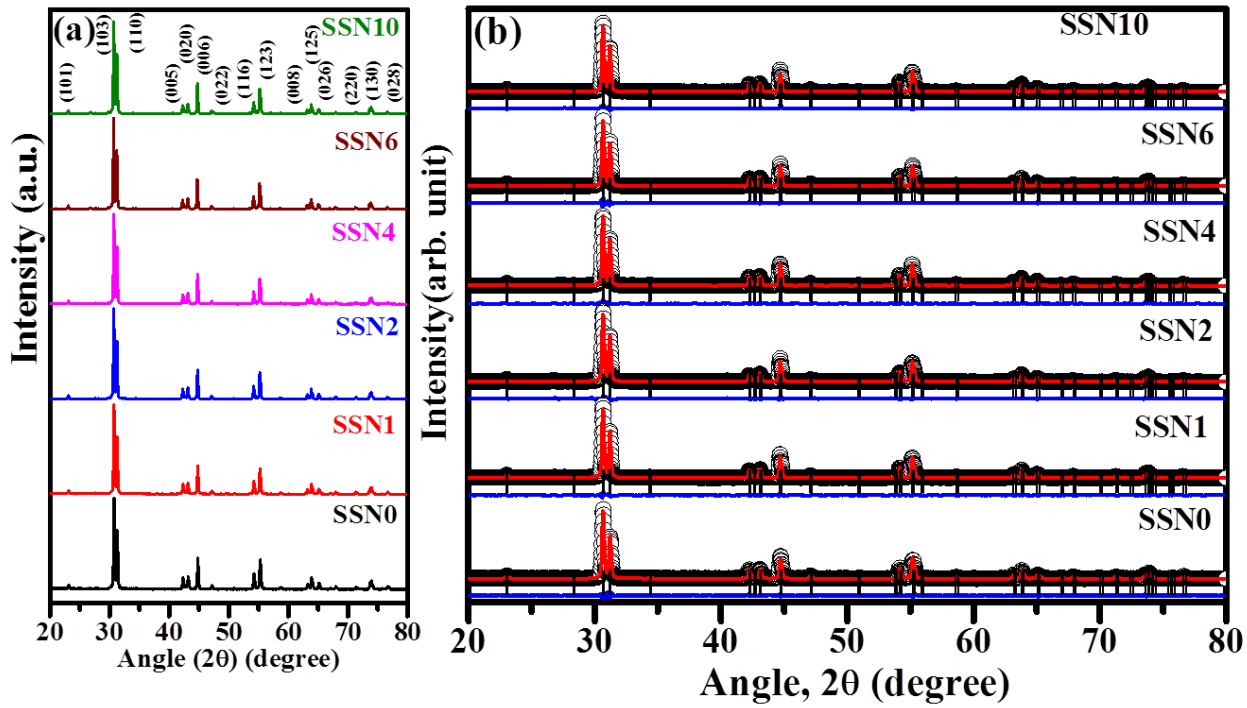

Figure 6.1 (a) Room temperature powder X-ray diffraction pattern of all samples. (b) The Rietveld refinement pattern of calcined powders. Here Yobs, Ycal, Yobs-Ycal and Braggs positions represent the experimental data, calculated data, the difference between both and Braggs position respectively.

The variation of lattice parameters (a and c) with dopant concentration (x) is shown in Figure 6.2(a). From Figure 6.2(a), it is noticed that the lattice parameter a (=b) increases with dopant concentration upto SSN4 thereafter, it remains almost constant for higher compositions. On the other hand lattice parameter c decreases upto SSN4 and remains almost constant for higher value compositions. The degree of distortion, R(=c/a) has calculated for the all samples and shown in Figure 6.2(b) against dopant concentration (x). The value of R is found to be decrease sharply upto SSN4 and thereafter, it becomes almost constant for above

compositions. The ionic radii of Nd^{3+} in 9th coordination is 1.16 Å which is lower than the ionic radii of Sr^{2+} in same coordination state i.e., 1.31 Å. Depending on the ionic radii the lattice parameters have to be decreased while parameters a=b is increased and c is decreased in present case. This result is similar to our earlier report discussed in Chapter 5. Decrease in the value of R might be due to decrements of lattice parameter c and increments of lattice parameter a(=b). However, occupancy of Sr in per unit volume of Sr_2SnO_4 higher along c-direction compared to a=b direction which results decrease in degree of distortion.

The broadening in the XRD peaks has contribution of various factors like crystallite size, lattice strain and instrumental broadening etc. After correction of instrumental broadening from the full width at half maxima of most intense peak (013), it is used to calculate crystallite size (D) by using Eq. (2.15) and listed in Table 6.1. From Table 6.1, it is observed that the crystallite size of doped samples is lower than the undoped sample. The Nd^{3+} at the Sr^{2+} site of the Sr_2SnO_4 is a donor; it is reported that donor doping in perovskite oxides inhibits grain growth. Hence, it results smaller crystallite size for doped samples which is consistent with the literature [23].

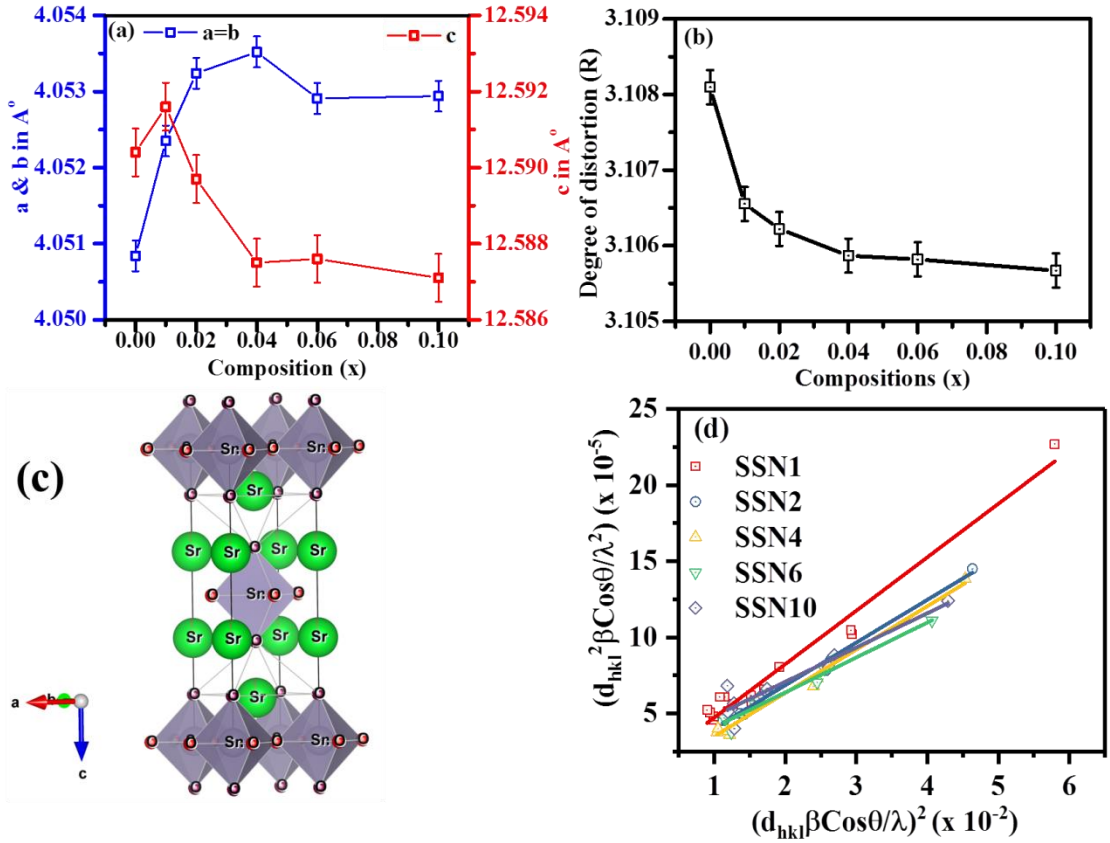

Figure 6.2 (a) Variation of lattice parameters (b) Degree of distortion (R=c/a) with composition. (c) Structure obtained using VESTA for sample SSN4 (d) SSP plot for all samples.

As discussed in Chapter 5, the crystallite size obtained from Debye Scherrer equation is not accurate. SSP plot technique has been used to determine crystallite size accurately [270]. Using Eq. (2.19), the plot of $\left(\frac{d_{hkl}\beta cos\theta}{\lambda}\right)^2$ vs. $\left(\frac{{d_{hkl}}^2\beta cos\theta}{\lambda^2}\right)$ for all samples are generated and shown in Figure 6.2(d). Using the value of intercept and slope the crystallite size and lattice strain are determined and given in Table 6.1. From Table 6.1, it is noticed that the value of crystallite size using SSP plot is slightly higher than the value obtained using Debye-Scherrer formula. This difference clearly reflects presence of lattice strain in samples. Higher value of lattice strain for doped samples may arise due to smaller ionic radii of Nd^{3+} ion (1.16 Å) in comparison the Sr^{2+} ion (1.31 Å).

Table 6.1 Rietveld refinement parameter, bond length, bond angle, crystallite size and lattice strain of all samples

Parameters	**SSN0**	**SSN1**	**SSN2**	**SSN4**	**SSN6**	**SSN10**
Lattice Parameters						
a=b	4.05084(6)	4.05324(4)	4.05352(8)	4.05235(5)	4.05291(6)	4.05294(8)
c	12.59040(18)	12.59160(14)	12.5897(16)	12.5875(17)	12.58760(13)	12.58710(11)
Angle (α,β,γ)	90=90=90	90=90=90	90=90=90	90=90=90	90=90=90	90=90=90
Rwp	20.4	11.1	9.56	9.86	10.9	13.6
Rp	16.7	10.2	8.86	9.32	9.79	12.2
$\chi 2$	4.17	4.1	3.2	3.1	2.8	4.8
R_{Bragg}	3.4327	4.29672	2.1848	1.79931	2.51429	3.05485
$S=R_{wp}/R_p$	1.22	1.09	1.08	1.06	1.11	1.12
Atomic Coordinate						
Sr	(0,0,0.35267)	(0,0,0.35300)	(0,0,0.35260)	(0,0,0.35230)	(0,0,0.35236)	(0,0,0.35152)
Nd	--	(0,0,0.35300)	(0,0,0.35260)	(0,0,0.35230)	(0,0,0.35236)	(0,0,0.35152)
Sn	(0,0,0)	(0,0,0)	(0,0,0)	(0,0,0)	(0,0,0)	(0,0,0)
O1	(0.5,0,0)	(0.5,0,0)	(0.5,0,0)	(0.5,0,0)	(0.5,0,0)	(0.5,0,0)
O2	(0,0,0.15754)	(0,0,0.15300)	(0,0,0.15862)	(0,0,0.16463)	(0,0,0.15824)	(0,0,0.15968)
Bond Length (Å)						
Sr-Sn (along a,b)	3.41255(3)	3.41811(5)	3.42141(6)	3.41574(6)	3.41567(7)	3.41456(3)
Sr-Sn (along c)	4.44015(15)	4.44483(11)	4.43913(8)	4.43458(3)	4.43537(8)	4.42462(15)
Sn-O1 (along a,b)	2.02538(4)	2.02662(5)	2.02676(3)	2.02698(3)	2.02645(5)	2.02647(7)
Sn-O2 (along c)	1.98344(7)	2.02472 (7)	2.02526 (5)	2.02651 (6)	2.02628 (6)	2.02605(8)
Bond Angle (degree)						
O1-Sr-O1	95.0314	95.18741	95.0449	94.9524	94.9231	94.6318
O2-Sr-O2	174.8608	176.9801	175.3572	174.4934	173.6687	172.3676
Crystallite Size (nm) and Lattice Strain						
Using Debye	49.30	48.11	45.42	41.65	46.85	44.38
Using SSP	51.20	50.65	49.65	46.24	48.52	47.84
Strain	3.00×10^{-3}	3.89×10^{-3}	4.17×10^{-3}	5.91×10^{-3}	6.94×10^{-3}	8.30×10^{-3}
Optical Band Gap (eV)						
Direct	4.74	4.88	4.85	4.83	4.80	4.78
Indirect	4.00	4.08	4.07	4.03	4.01	3.93

6.2.2 Transmission Electron Microscope (TEM) Analysis

The particle size of a sample is analyzed by transmission electron microscopy. TEM measurement is used to get the information of sample, size and presence of any secondary phase [271]. The morphology of one representative sample SSN4 is shown in Figure 6.3(a). From TEM analysis, it is observed that the particles are crystallized and agglomerated with

spherical morphology. The particle size distribution histogram obtained by using software "**Image J**" is shown in Figure 6.3(b). Average particle size is determined by fitting of Gaussian function to the histogram and found to be (45.12 ± 4.52) nm. The particle size is found to be slight higher than the crystallite size of same sample (Table 6.1), which indicates that single crystallites consists in one particle. Further, the high resolution TEM images of sample are shown in Figure 6.5(c). High resolution transmission electron microscope and selected area electron diffraction (SAED) patterns are used to probe the presence of desired phase. HR-TEM image illustrate that the lattice fringes are well developed and randomly oriented with respect to each other. The distances between two successive parallel lines of same orientation are calculated by **Image J** software. The spacing between the fringes is well matched by X-ray diffraction studies, which indicates that the obtained sample is single phase. Selected area electron diffraction (SAED) pattern shows bright spot in the form of a circular ring indicated the polycrystalline nature of sample. These rings belong to different Miller planes (h, k, l) are shown in Figure 6.3(i). The calculated d values from Figure 6.3(d-h) are 2.9017 Å, 3.1295 Å, 1.9218 Å, 3.8415 Å and 2.1282 Å are assigned to (013), (004), (022), (015) and (110) planes respectively of Sr_2SnO_4, which are consistent with XRD results discussed above [173].

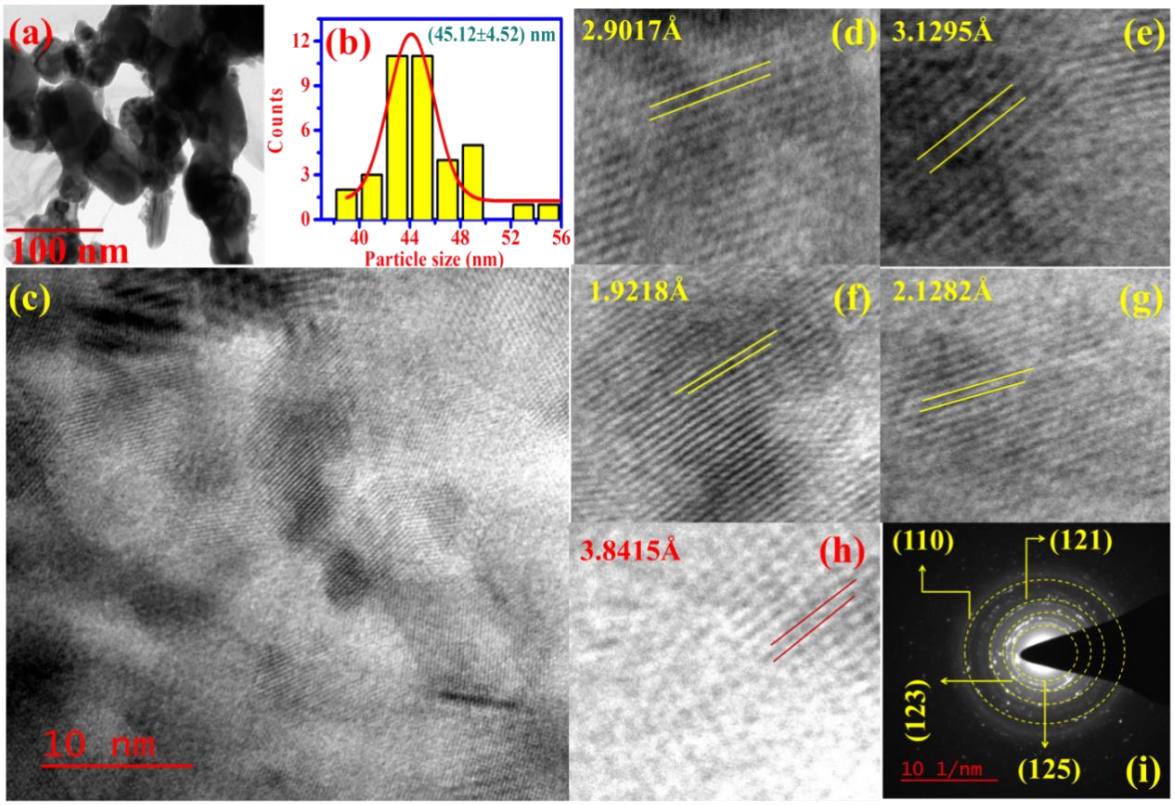

Figure 6.3 (a) Transmission electron micrograph of a representative sample SSN4, (b) Distribution function fitted with Gaussian Function (c) HR-TEM image of different crystallographic planes (d-h) and (i) Selected Area Electron Diffraction (SAED) pattern.

6.2.3 Raman Spectrum Analysis

The Raman spectroscopy is a simple and non-destructive tool to probe structural information to single unit cell level. In order to confirm the incorporation of Nd^{3+} ions in the lattice of Sr_2SnO_4 and detect impurity phases present in the trace amount. The Raman spectrum of all samples has been recorded in wavenumber range 100-1000 cm^{-1} is shown in Figure 6.4. Reitveld analysis confirmed that all the composition has tetragonal crystal structure space group $I4/mmm$ with symmetry group D_{4h}^{17} having two formula units per unit cell. According to group theory 14 modes are Raman modes given by Eq. (5.1) and only 4 modes are Raman active [243] present in all sample. The undoped sample SSN0 shows an intense Raman band splitted into two bands centred at 561 cm^{-1} and 581 cm^{-1} is observed due to vibration of oxygen in c-plane and in a/b-plane. With incorporation of Nd^{3+} at Sr^{2+} site, the bond length

associated with Sn-O1 and Sn-O2 is found to be almost equal (See Table 6.1). Due to almost similar bond length of Sn-O1/Sn-O2, the splitted bands merged into single band from sample SSN1 to SSN10. It is further noticed that with the incorporation of Nd, the position of Raman band observed at 561 cm^{-1} shift towards higher wavenumber which may be due to higher atomic mass (64 %) of Nd (144.2 amu) compared to Sr (87.62 amu) indicates the incorporation of Nd at Sr site in the sample.

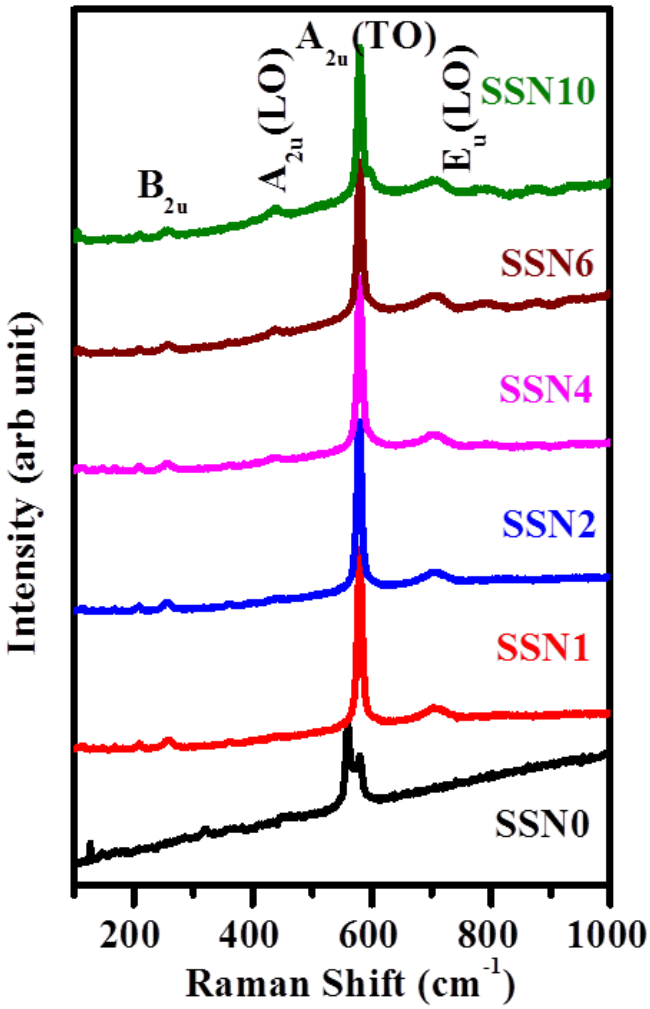

Figure 6.4 Room temperature Raman spectrum of all samples.

6.2.4 Fourier Transform Infrared Spectroscopy (FTIR) analysis

Fourier transform of Infrared (FTIR) technique has been employed to study the presence of various functional groups and changes in the vibrational bands due to the doping of Nd^{3+} at

the Sr^{2+} site in Sr_2SnO_4. FTIR spectra of the synthesized powders have been recorded in wavenumber range of 400-4000 cm^{-1} and are shown in Figure 6.5. As discussed in Chapter 3, two characteristics bands at 502 cm^{-1} and 726 cm^{-1} related to stretching modes of Sr-O and Sn-O_6 respectively are present [214]. The position of these characteristics bands shift with incorporation of Nd. The vibrational band of Sr-O stretching mode shifts towards higher wavenumber gradually with increasing concentration of Nd to 575, 579, 585, and 590 cm^{-1} for samples SSN1, SSN2, SSN4, SSN6 and SSN10 respectively. Moreover, it is observed that the stretching vibration of Sn-O_6 is unaffected with composition of Nd. It indicates that the substitution of Nd takes place at Sr^{2+}-site of Sr_2SnO_4 in the sample. Moreover, a weak band at 856 cm^{-1} indicate the presence of adsorbed CO_2 on surface of sample [214]. This band is diminishes with incorporation of Nd.

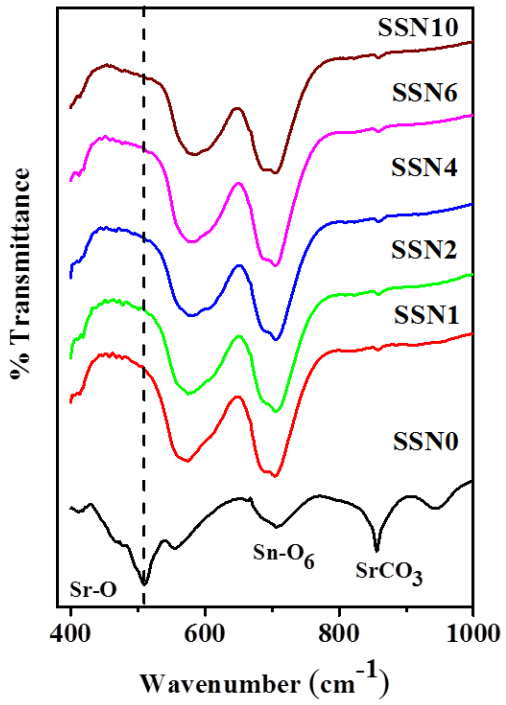

Figure 6.5 Fourier transform infrared (FTIR) spectra of all samples.

6.2.5 X-ray Photoelectron Spectroscopy (XPS) analysis

The X - ray photoelectron spectroscopic technique is used to reveal the valence state of the constituent element present in the composition SSN. In this work, we reported the XPS

spectrum of two samples SSN1 and SSN10. Figure 6.6 (a) shows the survey scan report of the sample SSN10 after C 1s correction. It contained peaks at 133, 284.6, 488.8, 531.6 and 980.8 eV attributed to the chemical states of Sr 3d, C 1s, Sn 3d, O 1s and Nd 3d state, respectively [184, 217]. Further, the valance states of various elements are determined from the High resolution XPS spectrum (HRXPS) for each element. Figure 6.6(b) depicts the HRXPS spectrum for Sr 3d. Two peaks positioned at 132.60 eV and at 134.35 eV have been fitted to core level spectra of Sr 3d for sample SSN1, while positioned at 132.82 and 134.57 eV for sample SSN10 to state Sr $3d_{5/2}$ and Sr $3d_{3/2}$ respectively. The separation between these peaks in both sample is 1.75 eV, indicates the existence of Sr in Sr^{2+} state [216]. Figure 6.6(c) shows the HRXPS spectrum of Sn 3d for both sample SSB1 and SSN10. It shows the doublet peak corresponds to $3d_{5/2}$ and $3d_{3/2}$ at 485.64 eV and 494.04 eV in sample SSN1 and at 485.80 eV and 494.20 eV in sample SSN10 [184, 216]. The broadening of peak with slight asymmetry towards lower binding energy side may be associated with multivalency of Sn. These peaks have been deconvoluted into two peaks. The first peak in $3d_{5/2}$ state is found at 484.60 eV and 485.71 eV and at 493.00 eV and 494.11 eV in $3d_{3/2}$ for sample SSN1 while for sample SSN10 it is observed at 484.93 eV and 493.33 eV in $3d_{5/2}$ state and 485.93 eV and 494.33 eV in $3d_{3/2}$ state respectively. In both the sample, the energy of separation between these peaks is almost constant i.e., 8.4 eV which indicates the presence of Sn. The peaks appeared at lower binding energy side is assigned to Sn in Sn^{2+} and higher binding energy to Sn^{4+} state [184]. Similarly, the HRXPS spectrum of Nd 3d is shown in Figure 6.6(d) for both samples. It show two peaks observed at 982.82 eV and 1005.22 eV for sample SSN1 and 984.36 eV and 1006.76 eV for sample SSN10 respectively. In both the sample, difference in the separation between the spin orbit states is remains same i.e., 22.4 eV. Position of these peaks is compared to literature and found that Nd ions are exist in Nd^{3+} state originated from Nd_2O_3 [272, 273]. Further, the core level spectra of O 1s for both the samples are shown in

Figure 6.6(e). The HRXPS spectra of O1s shows a single peak positioned at 530.37 eV for SSN1 and 530.58 eV for sample SSN10 respectively. The asymmetry in peak towards lower as well as higher binding energy side is observed for both samples which indicate the presence of different type of oxygen species. In order to know these oxygen species, the peak is deconvoluted in three peaks positioned at 529.00, 530.31 and 531.27 eV for sample SSN1, while at 528.86, 530.24 and 531.22 eV for sample SSN10. The peak appeared towards lower binding energy side is associated with the interstitial oxygen, and the peaks appeared thereafter is related to the O^{2-} associated with lattice oxygen while peak at higher binding energy side is attributed to oxygen vacancy. The presences of these defects were already described in Chapter 3 and Chapter 4 in terms of Kronger-Vink notation of defect.

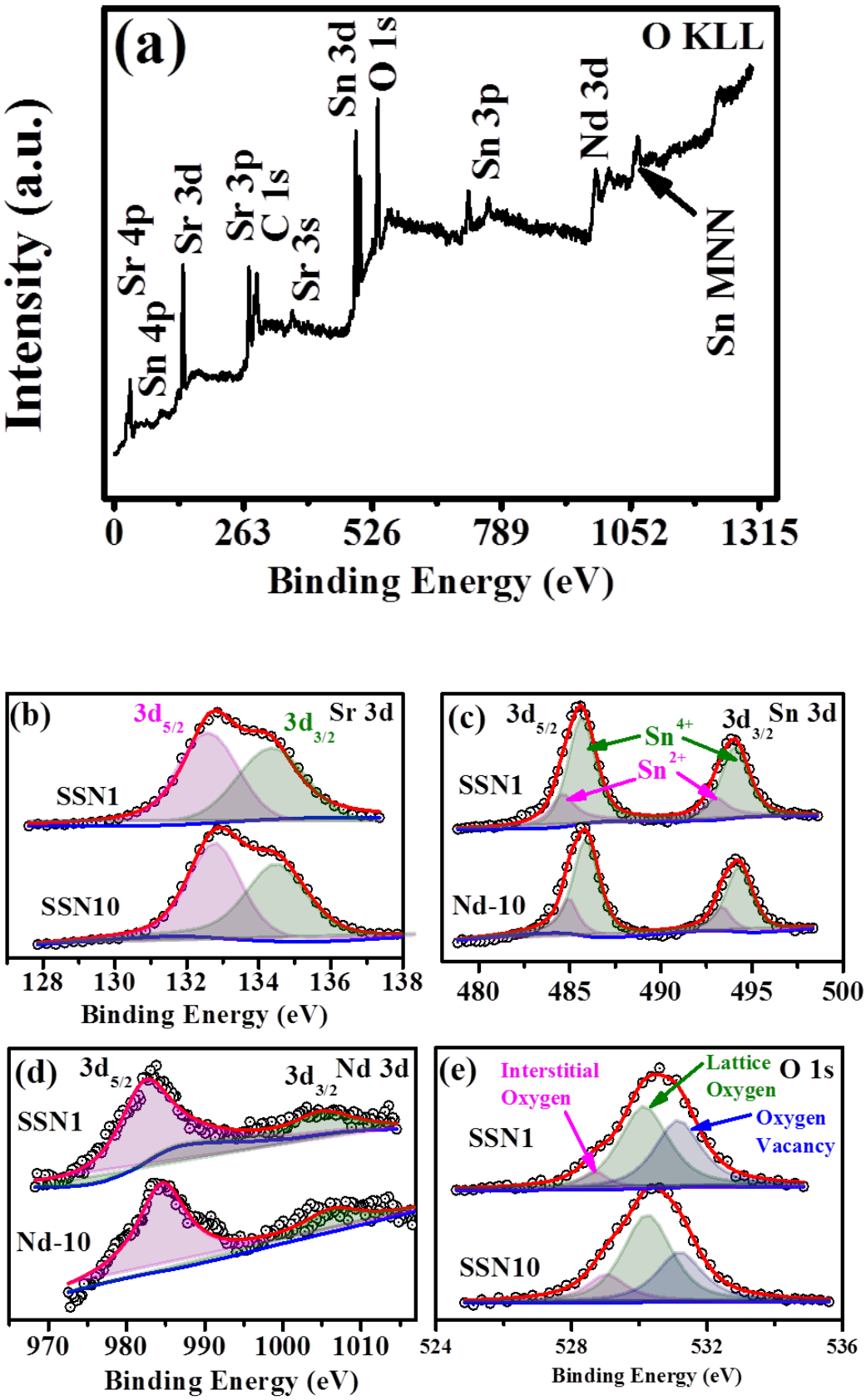

Figure 6.6 (a) Survey scan report for a sample SSN10, Core level XPS spectra of (b) Sr 3d (c) Sn 3d (d) Nd 3d (e) O 1s.

6.2.6 UV-Visible Spectroscopy analysis

The Ultraviolet-visible (UV) spectroscopy measurement has been probed to investigate the optical absorbance of Nd-doped Sr_2SnO_4. The room temperature absorbance UV spectra of all samples are depicted in Figure 6.7. The samples exhibit a strong absorption below 300 nm and their edge is lying in UV-region. The wavelength of absorbance edge is determined by extrapolation of linear region on the x-axis as shown in the inset of Figure 6.7. It can be seen from Figure 6.7, the absorption peak is shifted towards higher wavelength (Red Shift) side on incorporation of Nd. Furthermore, beside strong absorption edge in the UV range, few weak absorption edges are also observed in wavelength range from 350 to 800 nm. These edges are assigned by (i) to (xi) in the inset of Figure 6.7. This absorbance has assigned to transition between different energy level of f-shell of Nd^{3+}. On the basis of literature absorbance edges marked as (i), (ii), (iii), (iv), (v), (vi), (vii), (viii), (ix), (x) and (xi) belongs to transitions from $4I_{9/2}$ [274];

(i) $4I_{9/2} \rightarrow 4D_{5/2}$ (ii) $4I_{9/2} \rightarrow 4D_{1/2} + 4D_{3/2}$ (iii) $4I_{9/2} \rightarrow 2P_{1/2}$ (iv) $4I_{9/2} \rightarrow 2D_{3/2} + 2G_{9/2}$ (v) $4I_{9/2} \rightarrow 4G_{9/2} + 2K_{13/2}$ (vi) $4I_{9/2} \rightarrow 4G_{7/2}$ (vii) $4I_{9/2} \rightarrow 4G_{5/2}$ (viii) $4I_{9/2} \rightarrow 2H_{11/2}$ (ix) $4I_{9/2} \rightarrow 4F_{9/2}$ (x) $4I_{9/2} \rightarrow 4F_{7/2} + 4S_{3/2}$ (xi) $4I_{9/2} \rightarrow 4F_{7/2} + 2H_{9/2}$.

With increasing dopant concentration the absorbance in the same region gradually increases due to increasing Nd concentration in sample [275]. To estimate the optical band gap, the optical absorbance data has been analyzed in terms of Tauc relation as given by Eq. (2.21). The Tauc plot for both direct and indirect band gap of the samples are shown in Figure 6.8 (a-f). The optical band gap (both direct and indirect) determined using intercept of linear region on x-axis (Energy), where y=0. Obtained value of band gap (direct and indirect) are given in Table 6.1. From Table 6.1, it is noticed that value of direct band gap of doped samples is slight higher as compared to undoped Sr_2SnO_4. Slight higher value of band gap is may be ascribed to the lower crystallite size of sample (See Table 6.1). With concentration of

Nd, the direct band gap of doped samples gradually decreases. This might be due to presence of defect state $Nd_{Sr}^{\cdot}$ close to conduction band, which further become continuem state with increasing Nd and hence the direct band gap of the sample is decreased.

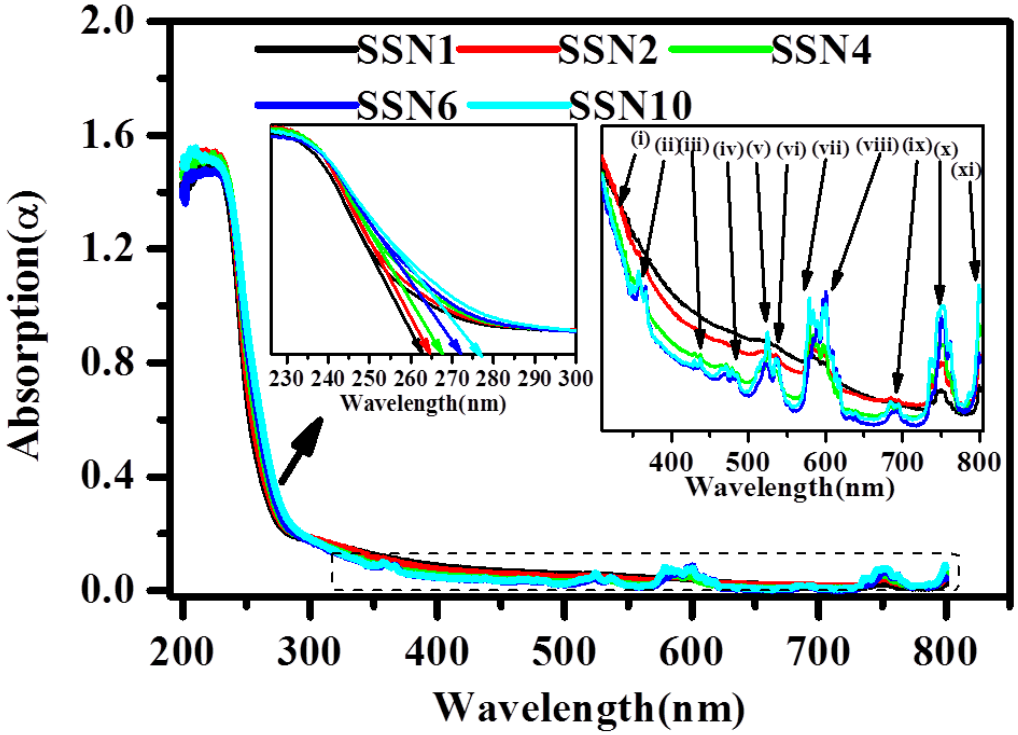

Figure 6.7 Room temperature absorbance spectra of SSN samples (Inset shows onset absorption and various absorption of Nd^{3+}.

From Table 6.1, it has been noticed that the value of the indirect band gap is lower than direct band gap for same composition. The lower value of indirect band gap may be due to the presence of defects such as oxygen vacancies (V_o^x, $V_o^{\cdot}$ and $V_o^{\cdot\cdot}$), lattice defects and distortion in local bond. Since difference in the both the band gap was almost lying in the range of (0.74-0.85) eV, which indicates the presence of same kind of defects. From the XPS analysis of the sample, it is found that oxygen vacancies (V_o^x, $V_o^{\cdot}$ and $V_o^{\cdot\cdot}$) are present in all sample which is found as common defects similar to other ceramic samples .

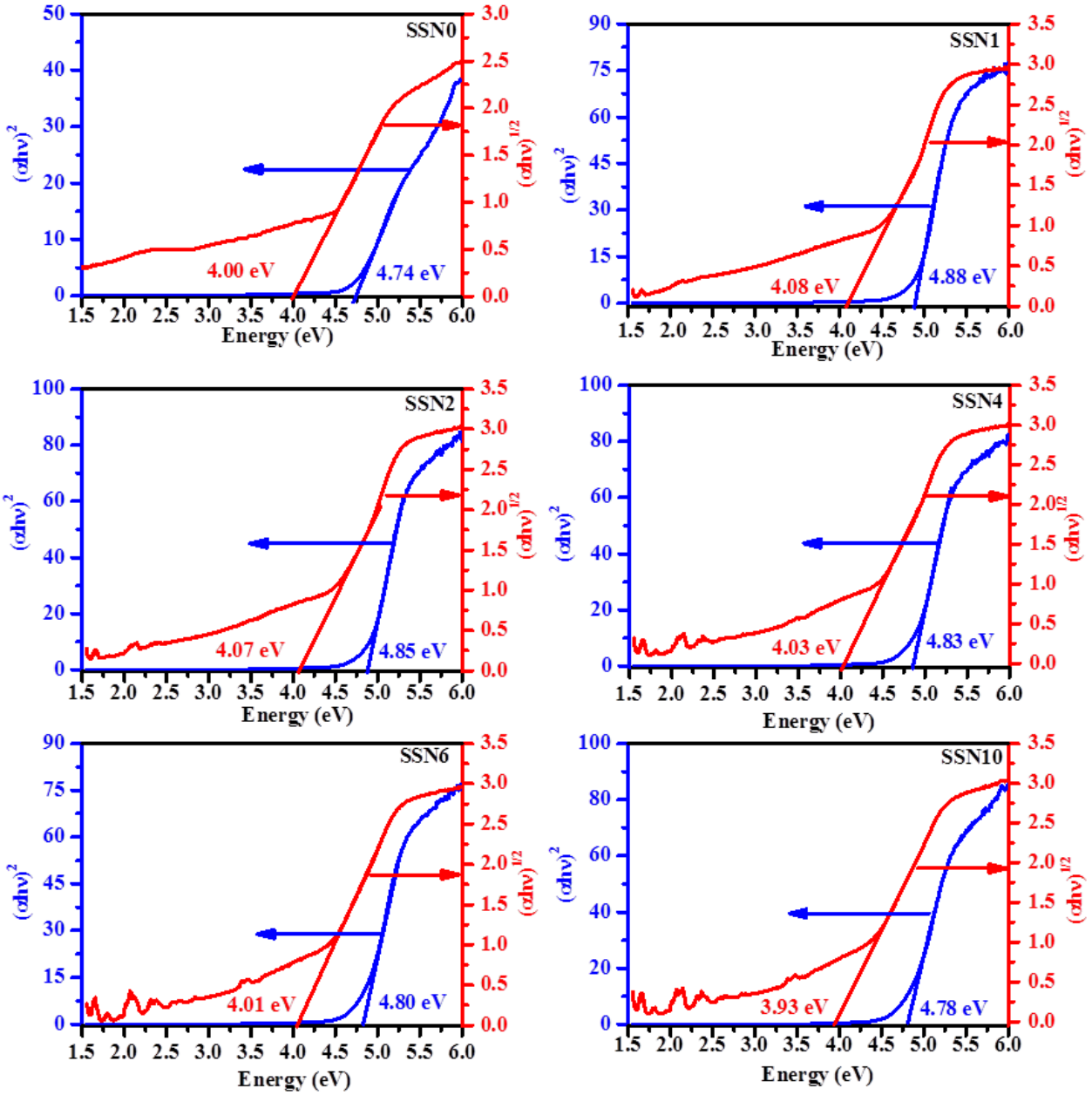

Figure 6.8 Tauc plot generated for both direct and indirect band gap of all SSN samples using Eq. (2.21).

6.2.7 Photoluminescence Spectroscopy analysis

To investigate the photoluminescence (PL) properties of sample at room temperature, the excitation spectra of all samples recorded within the wavelength range 200-800 nm are shown in Figure 6.9(a). From Figure 6.9(a) it is noticed that the excitation spectrum have few peaks observed at 266, 338, 474, 527, 592, 691 and 747 nm respectively, and their intensity

enormously increases with Nd concentration. First peak is attributed to direct band to band transition and others are due to transitions in Nd^{3+} which is similar to UV-Visible spectra. The peak appeared at 596 nm is most intense and sharp. Hence, the PL spectrums of doped samples are recorded using excitation wavelength of 596 nm and shown in Figure 6.9(b). The PL spectrum of all sample show 9 emission bands observed at 911, 923, 955, 987, 997, 1019, 1060, 1089, and 1121 nm respectively. There are two characteristic emission peaks of Nd^{3+} are observed in NIR region due to transitions, $4f_{3/2} \rightarrow 4I_{9/2}$ and $4f_{3/2} \rightarrow 4I_{11/2}$ observed at 911 nm and 1060 nm respectively [274]. For transition $4f_{3/2} \rightarrow 4I_{9/2}$, five lines are expected for one Nd^{3+} sites and two lines for $4f_{3/2} \rightarrow 4I_{11/2}$ [275]. In present case total 9 lines are observed. The large number of transitions in present sample is may be due to presence of multiple luminescence centres for Nd^{3+} sites in Sr_2SnO_4 (One is within perovskite $SrSnO_3$ and other in layer SrO). The most prominent peak appeared in PL emission spectra at 1064 nm makes it a promising candidate for near infrared (NIR) luminescence devices.

In order to determine the optimum concentration of Nd in Sr_2SnO_4, the most prominent peak appeared at 1060 nm is considered. The intensity of emission peak is increasing with increasing concentration of Nd upto SSN6 and thereafter, it decreased. From this variation, the optimum concentration of Nd in SSN sample is found to be 6% which is also known as critical concentration. The further increase of Nd leads decrease in luminescence intensity which is termed as concentration quenching. The concentration quenching effect occurred due to non radiative energy transfer between Nd^{3+}-Nd^{3+} ions.

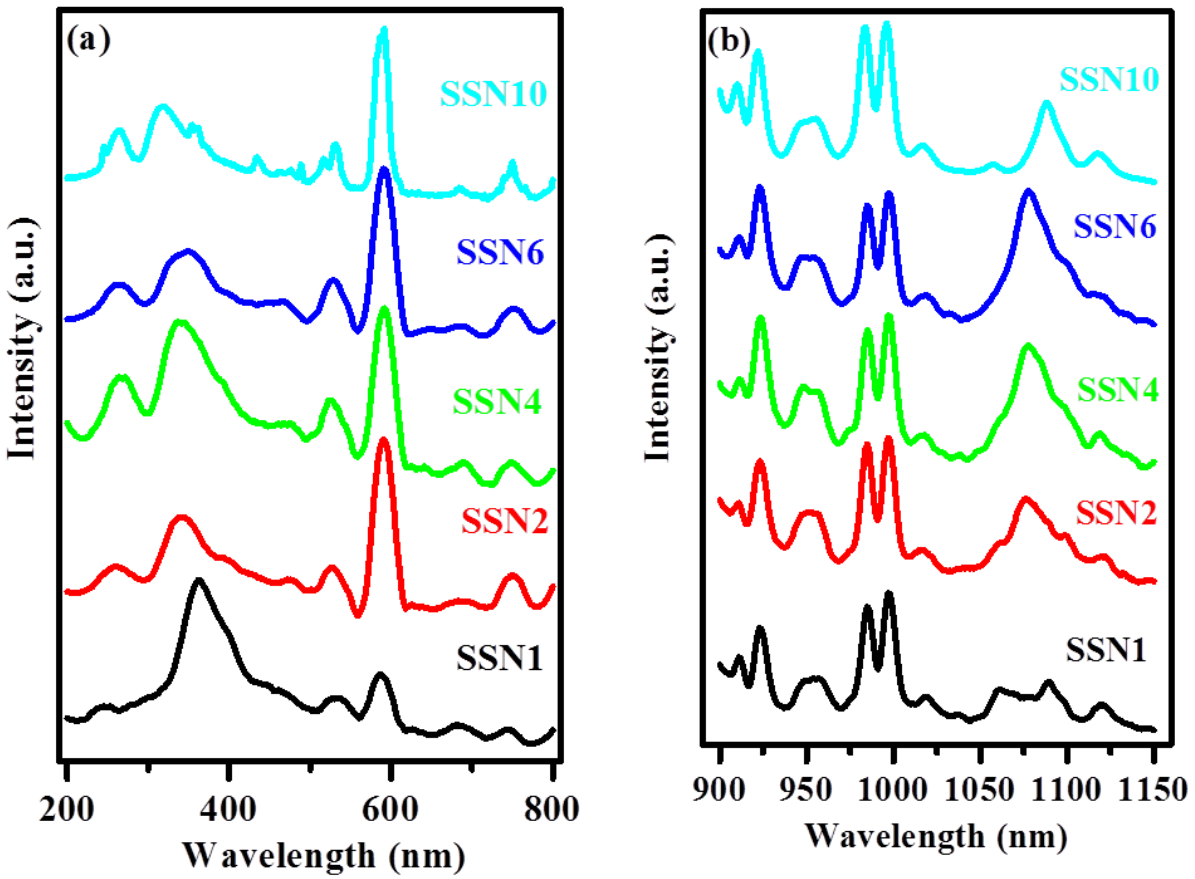

Figure 6.9 (a) Room temperature excitation spectra of samples for emission $\lambda_{emi.} = 1060\,nm$ (b) Room temperature emission spectra for all samples under excitation wavelength $\lambda_{exc.} = 596\,nm$.

6.2.8 Magnetic Characterization

To explore the magnetic properties of SSN samples, the vibrating sample magnetometer measurement has been performed under the applied magnetic field ± 40 kOe. The room temperature magnetization vs. magnetic field intensity (M-H) curve of all the samples is shown in Figure 6.10. It can be seen from the curve that the sample SSN0 exhibits a diamagnetic behaviour at high field with a very weak ferromagnetic behaviour at low field. Incorporation of Nd in SSN sample results suppression of diamagnetic behaviour which can be seen for SSN1. On further increase in the concentration of Nd, the magnetization increases and become ferromagnetic for SSN2. In sample SSN2, a perfect ferromagnetic hysteresis loop with a well-defined saturation magnetization i.e., Ms=0.026 emu/gm is observed.

However, M-H curve of samples SSN4, SSN6 and SSN10 contained a hysteresis loop at low magnetic field, while it is almost linear at higher magnetic field. The linear nature M-H curve at high magnetic field indicates the presence of paramagnetic or antiferromagnetic ordering in the samples. Presence of hysteresis loop with coercive field in all sample rules out the possibility of paramagnetic interaction in sample. The value of remanent magnetization (M_r), saturation magnetization (M_s) and coercive field (H_c) obtained from M-H curve of all sample are given in Table 6.2. From Table 6.2, it is noticed that initially the value of saturation magnetization (M_s) increases from sample SSN0 to SSN2 and then decreased for SSN4 and then gradually increases with Nd upto SSN10. Similar trend is observed for the value of remanent magnetization. The value of coercive magnetic field is almost same for all samples.

Table 6.2 Magnetic parameters obtained from M-H curve of samples**.**

Sample	Mr(x 10^{-3}) emu/gm	Ms(x 10^{-3}) emu/gm	Hc
SSN0	0.003	0.09	38
SSN1	0.163	4.15	20
SSN2	0.234	26.21	10
SSN4	0.098	13.78	18
SSN6	0.078	17.36	19
SSN10	0.062	35.11	23

Origin of Ferromagnetism

Room temperature ferromagnetism observed for many oxides has been well explained by Coey et al. Presence of oxygen vacancy is already probed from XPS analysis of samples. Undoped Sr_2SnO_4 shows the presence of weak ferromagnetism at low magnetic field and diamagnetic at high magnetic field. In many oxide ceramics the origin of ferromagnetism is explained in terms of oxygen vacancies which promote ferromagnetic ordering via ($Sn^{2+} - V_{\ddot{O}} - Sn^{4+}$) in the sample [239]. Since from Figure 6.10, it is noticed that all doped sample exhibit ferromagnetism at room temperature which suggests the presence of ferromagnetic

ordering ($Sn^{2+} - V_{\ddot{O}} - Sn^{4+}$) in all samples. From Table 6.2, it is observed that the value of saturation magnetization gradually increased to 26.21 x 10^{-3} emu/gm for SSN2 which might indicates the presence of additional ferromagnetic ordering in the sample. Since Nd^{3+} acts as donor at Sr^{2+} site and the charge neutrality takes place according to following equation.

$$Nd_2O_3 \xrightarrow{Sr_2SnO_4} 2Nd_{\dot{S}r} + 2e' + 3O_O^x \quad (6.1)$$

From above equation, it is found that the doping of Nd does not favour the formation of oxygen vacancy, while it favours the formation of Sn^{2+}, i.e., $Sn^{2+}{}_{Sn^{4+}}{}''$. Surprisingly the order of magnetization increases upto 10^2 orders which indicate presence of strong ferromagnetic ordering (compared to undoped) in the sample. Ferromagnetism in Gd-doped CeO_2 is explained by interaction between Ce^{3+}-Ce^{4+} through super-exchange mediated via oxygen vacancy [276]. Presence of oxygen vacancy in various oxide ceramics doped with transition metal gives ferromagnetism mediates either by double exchange or by super-exchange mechanism [47, 259, 277–280]. In present case, there are two kinds of interaction are possible by Nd doping such that the first one is ($Nd^{3+} - V_o{}^{\ddot{}} - Sn^{2+}$) and second one is ($Nd^{3+} - V_O{}^{\ddot{}} - Nd^{3+}$) [276]. The ordering in ($Nd^{3+} - V_o{}^{\ddot{}} - Sn^{2+}$) by super-exchange mechanism favours ferromagnetism while ordering in ($Nd^{3+} - V_O{}^{\ddot{}} - Nd^{3+}$) favours antiferromagnetic ordering in sample [281]. From Table 6.2, it is noticed that value of the saturation magnetization increases gradually upto sample SSN2 which may be possible due to increase of ferromagnetic ordering via ($Nd^{3+} - V_o{}^{\ddot{}} - Sn^{2+}$), which is mediated via oxygen vacancy by either double exchange or super-exchange [277]. Thereafter, the value of saturation magnetization decreased for sample SSN4 which may be because of the domination of antiferromagnetic ordering ($Nd^{3+} - V_O{}^{\ddot{}} - Nd^{3+}$) over ferromagnetic ordering $\left(Nd^{3+} - V_o{}^{\ddot{}} - Sn^{2+}\right)$ in sample. According to antiferromagnetic ordering, the two spins have equal magnitude aligned antiparallel to each other as (↑↓), and with further increase in antiferromagnetism the overall resultant is increases. Value of the saturation

magnetization is then gradually increased with Nd is may be due to increase in antiferromagnetic ordering via $(Nd^{3+} - V_o^{\cdot\cdot} - Sn^{2+})$ in the sample. Thus, the value of saturation magnetization increased.

The value of remanent magnetization is increasing gradually upto SSN2 attributed to the presence of ferromagnetic interaction in the sample. Thereafter, value of the remanent magnetization is decreased with further increasing of dopant concentration Nd which may be because of antiferromagnetic ordering $(Nd^{3+} - V_O^{\cdot\cdot} - Nd^{3+})$ in sample which results decrease the value of remanent magnetization.

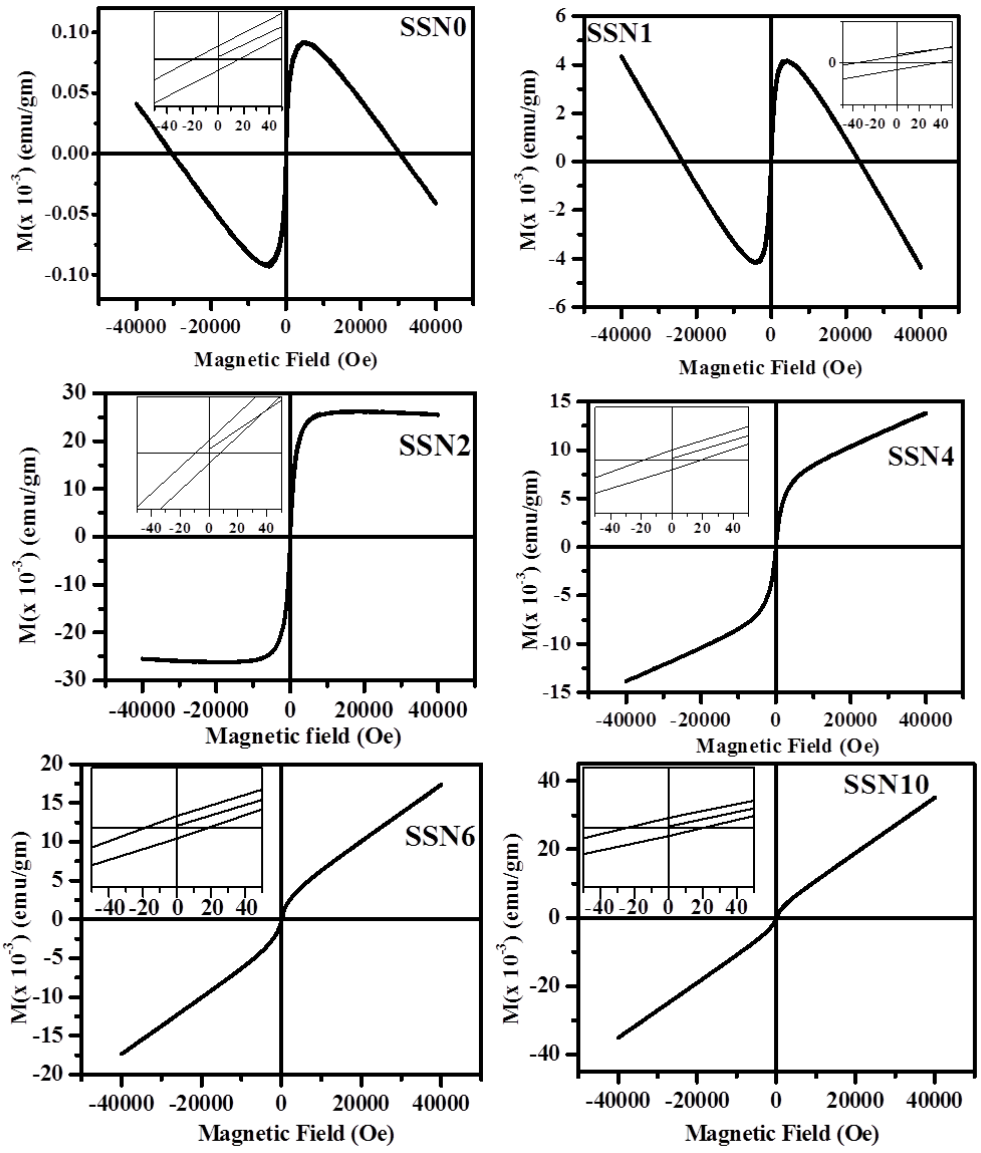

Figure 6.10 Room temperature M-H curve for all samples.

6.3 Conclusions

The samples of SSN compositions were prepared by solid state reaction route by calcining at 1000^{o}C for 8h. The obtained samples were further analyzed using XRD, Raman and FTIR spectroscopy. The XPS analysis of the sample reveals the presence of Sn in Sn^{2+} state oxygen vacancies in the sample. UV-Vis spectroscopy of all the samples further confirmed the incorporation of Nd^{3+} in the sample. Room temperature PL spectra of doped samples exhibit an intense emission around 1064 nm assigned to transition $4f_{3/2} \rightarrow 4I_{11/2}$ of Nd^{3+}, which can be utilized for NIR luminescence device application. The magnetic properties of the doped samples were studied to explore their applications in spintronics. Undoped sample exhibit weak ferromagnetic behaviour at low magnetic field and diamagnetic behaviour at high magnetic field. Doping of Nd diminishes diamagnetic behaviour and increased gradually ferromagnetic behaviour upto SSN2 due to ferromagnetic ordering between ($Nd^{3+} - V_o^{\cdot\cdot} - Sn^{2+}$). The SSN2 sample found to be ferromagnetic in nature with dilute ferromagnetism 0.024 emu/gm. Further, increase of Nd induced antiferromagnetic ordering in the samples and the sample exhibit typical antiferromagnetic in nature. The small value of saturation magnetization makes it suitable candidate for dilute magnetic semiconductor applications.